Structure of trailing vortices: Comparison between particle image velocimetry measurements and theoretical models

C. del Pino,[1] L. Parras,[1] M. Felli,[2] and R. Fernandez-Feria[1]

[1]*E. T. S. Ingenieros Industriales, Universidad de Málaga, Dr Ortiz Ramos s/n, 29071 Málaga, Spain*
[2]*Propulsion and Cavitation Lab, INSEAN, Via di Vallerano 139, 0128 Rome, Italy*

The velocity field of the trailing vortex behind a wing at different angles of attack has been measured through the stereo particle image velocimetry technique in a water tunnel for Reynolds numbers between 20 000 and 40 000, and for several distances to the wing tip. After filtering out the vortex meandering, the radial profiles of the axial and the azimuthal velocity components and of the radial profiles of the vorticity were compared to the theoretical models for trailing vortices by [G. K. Batchelor, J. Fluid Mech. **20**, 645 (1964)] and by [D. W. Moore and P. G. Saffman, Proc. R. Soc. London, Ser. A **333**, 491 (1973)], whose main features are conveniently summarized. We take into account the downstream evolution of these profiles from just a fraction of the wing chord to more than ten chords. The radial profiles of the vorticity and the azimuthal velocity are shown to fit quite well to Moore and Saffman's trailing vortex model, while Batchelor's model does not fit so well, especially in the tails of the profiles. At the downstream distances considered, the radial profiles of the axial velocity do not adjust so well to Moore and Saffman's model as the azimuthal velocity profiles do, but the disagreement with Batchelor's model is quite manifested, especially at the axis. Thus, the details of the flow structure are in better agreement with the predictions of Moore and Saffman's model. The downstream evolution of several key features of the measured velocity profiles is also in agreement with the predictions of Moore and Saffman's model, within the dispersion of the experimental data, but up to the largest axial distance considered in this work we cannot decide if they follow the asymptotic behavior predicted by this model. © *2011 American Institute of Physics*. [doi:10.1063/1.3537791]

I. INTRODUCTION

The precise knowledge of the dynamics, and the control, of trailing vortices in the wake behind commercial aircrafts are relevant problems in civil aviation, for these vortices strongly affect the frequencies of taking off and landing of aircrafts in an airport.[1–3] Many recent numerical and experimental researches have investigated the behavior of aircraft vortices, aiming at their characterization and the search for means of reducing the associated hazard (e.g., Refs. 4–7). Within these investigations, one of the main lines of research is about the role of vortex instabilities on wake decay and control.[8–13] However these works also show that the hydrodynamic stability predictions strongly depend on the precise structure of the models used for these trailing vortices, particularly on the sometimes neglected axial flow, hence the relevance of acquiring accurate experimental measurements of trailing vortices behind aircraft wings that may allow for an assessment of the best theoretical models from which to analyze the stability of these wake vortices. This is the main objective of the present work.

Other technological applications that may benefit from the precise knowledge of the structure of wing tip vortices are the problem of reducing the lift induced drag originated by tip vortices, the optimization of the tip vortex interaction with rotor blades in helicopters and propellers, which causes rotor blade fatigue failure and excessive rotor blade noise,

and the minimization of the hazard during aerial refueling of a fighter aircraft by a tanker, among others.[14]

There exists a very abundant literature, from the 1960s and even earlier, on the structure of trailing vortices. Here, only the most relevant ones for our work are mentioned. The first serious model on the structure of trailing vortices, taking into consideration the axial velocity component, was published by Batchelor.[15] A simplified "parallel" version of that vortex model (i.e., neglecting the downstream axial variation of the vortex), usually called "q-vortex,"[16] has been used since then as the base flow of numerous stability analysis of trailing vortices (e.g., Refs. 9–11 and 16–21, to mention just a few relevant, and a few recent, works). After Batchelor's work, several others models were developed based on the experimental visualizations and quantitative measurements undertaken by McCormick *et al.*,[22] Olsen,[23] and especially those by Saffman's group in Pasadena,[24] which utilized the, by that time just developed, technique of Laser Doppler Anemometry (LDA). Moore and Saffman[25] developed a model taking into account the roll-up process in the formation of the trailing vortices, extending Batchelor's model to azimuthal velocity profiles decaying as an arbitrary power of the radius of the vortex. Recently, Chadwick[26] published a trailing vortex model based on a similar approach as Batchelor's, with the same q-vortex structure on a given plane perpendicular to the vortex axis, but with a different decay of the axial velocity. It is also worth mentioning here the two-core scales vortex model of Fabre and Jacquin,[8] which, as a

23, 013602-1

difference with those commented on above, is a two-dimensional vortex with no axial flow and, therefore, a generalization of the Lamb–Oseen (Gaussian) vortex, but having the property of decaying differently to a potential vortex in the inner core, as in the vortex model considered by Moore and Saffman.[25] The flow structure given by the most relevant of these models for wing tip vortices will be described with some detail in Sec. IV A, in the context of the reported experimental results.

On the other hand, experimental measurements of isolated wing tip vortices have been performed by several authors. In particular, the near-field structure has been measured using different experimental techniques.[27–30] Experimental measurements several chords downstream, which are more relevant for the present work, have been recently made, using LDA and/or particle image velocimetry (PIV) techniques, by Devenport *et al.*[31] and by Roy.[32] These authors fitted their experimental results to a q-vortex model and to a two-core scales vortex model, respectively. However, these measurements were only taken at fixed axial locations of the vortex, without any attempt to obtain the axial variation of the velocity field, which constitutes one of the main objectives of the present work. The knowledge of this axial dependence of the velocity components is important to decide about the family of vortex models fitting the experimental measurements.

One of the main difficulties of measuring the velocity field in a wing tip vortex is the *meandering* phenomenon, or random fluctuation of the vortex centerline. This meandering is quite significant a few chords downstream of the wing, but it is less pronounced within a chord from the trailing edge. A consequence of the meandering, also called *wandering*, phenomenon is that vortices measured by static measuring techniques appear to be more diffuse than in reality, so that a correction method is needed.[31,33,34] The meandering was originally thought to be due to free-stream turbulence.[24] Then it was understood to arise from an instability of the vortex core.[14,35] However, recent work on transient energy growth through an optimal perturbation analysis and a stochastic forcing analysis[36] shows that the very long wavelength observed in the meandering of wing tip vortices can be explained by a resonant excitation due to noise located outside of the vortex core.[37] Recent experimental studies have corroborated this connection between free-stream turbulence and the amplitude of vortex wandering.[34,38] Therefore, vortices are very sensitive to even very small intrusive probes, and only nonintrusive techniques such as LDA or PIV yield consistently reliable data on the vortex structure. On the other hand, the strong unsteadiness of the core flow and the small vortex core dimension mitigate against the use of anything but global, nonintrusive measuring techniques. For these reasons we use the PIV technique in this work for measuring the velocity field in trailing vortices, complemented with statistical analysis of the experimental data to locate the vortex centerline and to correct the measured velocity field.

II. EXPERIMENTAL SETUP

The experiments were performed in a large horizontal water tunnel in the Laboratory of Aero-Hydrodynamics at the University of Málaga, with a working section of 0.5×0.5 m^2 cross-section and 5 m long. The designed velocity range in this hydrodynamic tunnel is 0–0.75 m/s, which is achieved through two centrifugal pumps of 18.5 kW each. Its turbulence level is less than 3%. The flow rate is measured through a turbine flow meter with a nominal resolution of less than 0.5%, located downstream of the pump. This flow meter was calibrated previously to the experimental results reported below through axial velocity measurements using a LDA technique, and through velocity measurements on a plane parallel to the mean stream using a two-dimensional PIV technique.

To generate the wing tip vortices we used a model with a NACA 0012 wing profile, with a chord $c = 10$ cm and with a rounded (half-circular) tip, vertically mounted on the upper surface of the first sector of the channel working section, in such a way that the wing tip was approximately at the center of the test section. This wing model was mechanized in aluminum, and painted with a special pigment to avoid or minimize corrosion by water. We have selected this particular wing model because it is the commonest one used in previous experimental works on the wing tip vortex (e.g., Refs. 31–34). Of course, the particular rounded tip geometry has an influence on the flow, especially on the roll-up process close to the wing tip. However we have not checked this point because we have only used this geometry. We believe that the influence of the rounded tip geometry becomes negligible sufficiently far from the wing tip.

The wing model was attached to the upper surface of the tunnel working section through a circular window specially designed and built to allow for the rotation of the wing into several positions, thus making possible the configuration of different angles of attack between the upstream flow and the wing. In addition, this window was provided with a connection between a system of controlled injection of dye and the wing, permitting flow visualizations in the wake behind the wing tip, which complemented the PIV measurements reported below.[39]

We used a "stereo" PIV system for measuring the three-dimensional (3D) velocity field at different cross sections of the wing tip vortex. As it is well known, the PIV technique consists of the accurate, quantitative measurement of fluid velocity vectors at a very large number of points by tracking, registering, and processing the successive positions of particles inoculated into the flow (see, e.g., Refs. 40–42). Stereo or 3D PIV is used to obtain the three-component velocity field in the planar region illuminated by a laser light sheet. The fundamental principle behind 3D PIV is stereoscopic imaging of particles in an illuminated plane in the flow. Two cameras view the plane at different angles and capture particle displacement images that contain the influence of the third velocity component. Data reduction algorithms provide the true particle displacements and on-line 3D velocity vector field display.

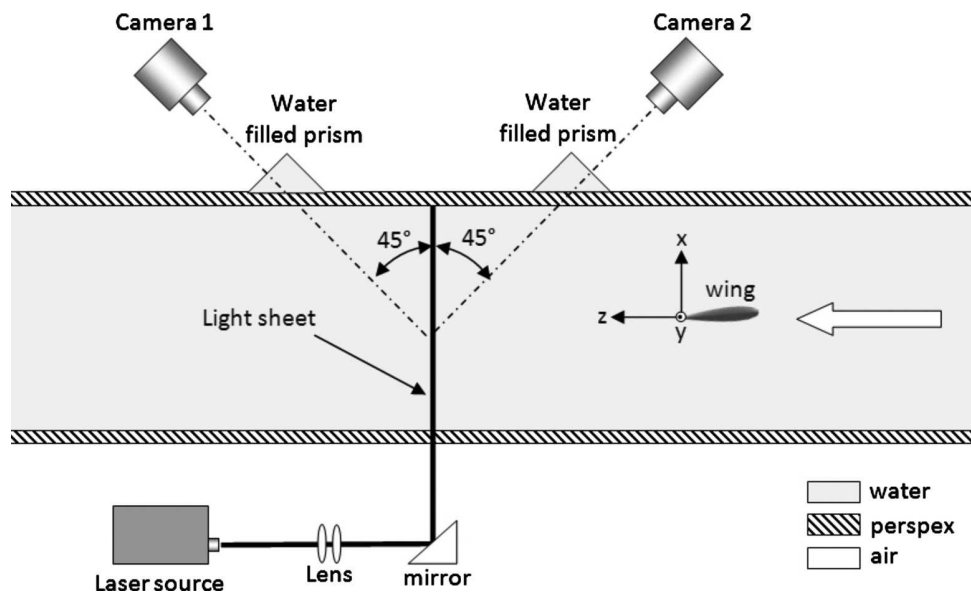The stereoscopic PIV system used in this work consists

FIG. 1. Sketch of the PIV-tunnel configuration used in the 3D measurements of the velocity field. Note that both cameras are on the same lateral side of the tunnel working section.

of a double pulsed Nd:yttrium aluminum garnet laser (150 mJ/pulse standard), two charge-coupled device cameras of 4 megapixels each and a synchronizer. To create the laser sheet a cylindrical lens was used. The particles inoculated into the flow for capturing the velocity field through the PIV system were hollow glass spheres with 10 μm diameter (HGS-10 from Dantec). These particles are neutrally buoyant in water, thus minimizing their relative motion to the water flow due to gravity and centrifugal forces. We did not observe in the PIV images any appreciable particle depletion in the vortex core due to centrifugal forces.

In order to minimize the effect of refraction, two transparent (Plexiglas) prismatic windows were attached to the lateral sides of the channel working section (see Fig. 1). These windows, which faced normally the cameras by forming an angle of 45° with the Plexiglas walls of the channel, were filled with water and adjusted through watertight unions to the channel walls.

We adopted a configuration of the PIV system in which both cameras recorded forwardly scattered light emitted from the PIV particles in the measuring plane (see Fig. 1). The intensity of forward scatter light is much larger than that from backward scatter,[41] and with this configuration much better results were obtained than with the first configuration that we used, in which each camera was located on a different side of the tunnel working section.

III. EXPERIMENTAL RESULTS

We have measured the 3D velocity field on normal (x, y)-planes to the axial mean flow in the water tunnel (z-direction; see Fig. 1) located at six different axial distances downstream of the wing tip ($z/c = 0.5, 3, 4, 6, 12.5,$ and 16), for three different angles of attack ($\alpha = 6°, 9°,$ and 12°), and for two different flow rates through the tunnel ($Q \simeq 38,$ and 83 l/s, measured by the flow meter downstream of

the pump mentioned above) that fixes the two Reynolds numbers considered. The different values of the parameters are summarized in Fig. 2. The Reynolds number based on the wing chord c, defined as

$$Re_c = \frac{W_\infty c}{\nu}, \tag{1}$$

where W_∞ is the measured upstream mean velocity and ν the kinematic viscosity of water, varied from approximately 2×10^4 for the lowest flow rate to 4×10^4 for the largest flow rate. The errors bars in Fig. 2 take into account the fluctuations of the measured flow rate during the PIV measurements in each case. For the Reynolds number, the fluctuations in the measured temperature were also taken into account through the kinematic viscosity. We looked for an averaged constant Reynolds number, so that in some cases we had to change slightly the upstream velocity due to ambient temperature changes (see, for instance, Fig. 2).

The parameters used for capturing images with the stereo PIV cameras were the following: PIV exposure 510 μs,
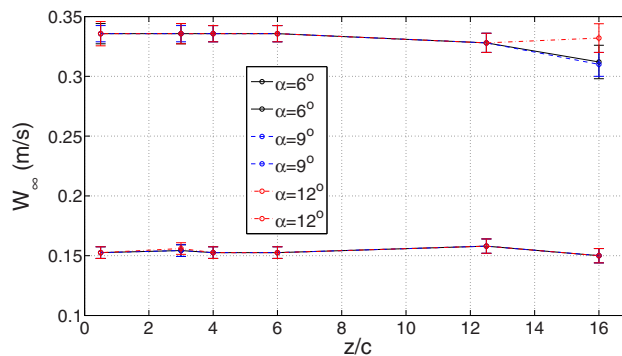

FIG. 2. (Color online) Measured mean upstream velocity W_∞ for the different axial distances z/c and angles of attack α considered.

laser pulse delay 425 μs, and $\delta t = 600$ μs. The determination of the three velocity components in the measurement plane requires the processing of the images captured by the left and the right cameras at each instant of time. There exist different techniques to perform this image processing. In order to be confident with the measured experimental results that we compare to the theoretical models, we have used three different procedures in a number of cases, and then we have compared the different results. In particular we have used the software INSIGHT 3G for stereo PIV from the company TSI that supplied our PIV equipment;[43] a technique developed by Meunier and Leweke,[44] but extended by us from two-dimensional (2D) PIV to 3D velocity fields, which uses a MATLAB-based software and has proven to be very effective for measuring the 2D velocity field of vortices,[45,46] and, finally, a more sophisticated technique developed at IN-SEAN by Di Florio *et al.*,[47] also appropriate for large velocity gradients, that first preprocesses the images captured by the cameras, thus allowing better results with poor PIV images. All these techniques compute the three velocity components in each measurement plane, including the (small) radial velocity component that will not be shown in the results reported below.

For a given case (i.e., for a given z/c, Re_c, and α) we captured and processed the data for 450 instants of time. Once the images have been processed by any one of the above mentioned techniques, the next step is to center the (x, y) coordinates of each one of these images at the center of the vortex, which is identified cross correlating the vorticity with a Gaussian distribution around its maximum value, and then average the velocity and vorticity fields using all the valid images taken for a given configuration. For this averaging process we used a square region of 2×2 cm^2 centered at the vortex axis. This recentering and averaging process was made with a MATLAB-based software, and it is essential to obtain a mean velocity field that filters out the meandering phenomenon on a given plane normal to the vortex axis.

In some sample cases we have processed the PIV images by the three techniques mentioned above, and have compared the resulting mean velocity components and vorticity. We found that the results from the three different image processing techniques are very similar, especially for the azimuthal velocity component and the vorticity, the differences being within the experimental errors (see Fig. 3 for a given case). This fact makes us confident about the 3D velocity field of the wing tip vortices measured here, taking into account that the most elaborate image processing technique by Di Florio *et al.*[47] (Imag. Proc. III in Fig. 3), which includes a preprocessing of the raw PIV images, yields practically the same mean velocity profiles than the other two techniques, especially when compared to the image processing technique based on the method by Meunier and Leweke[44] (Imag. Proc. II in Fig. 3). For the subsequent comparison with the theoretical models (Sec. IV) we use the results obtained with this last mentioned image processing technique based on the method by Meunier and Leweke. The reason is two-fold: first because the total computer time needed for processing the images, including the recentering and averaging processes, is much smaller than with the other techniques, mainly because
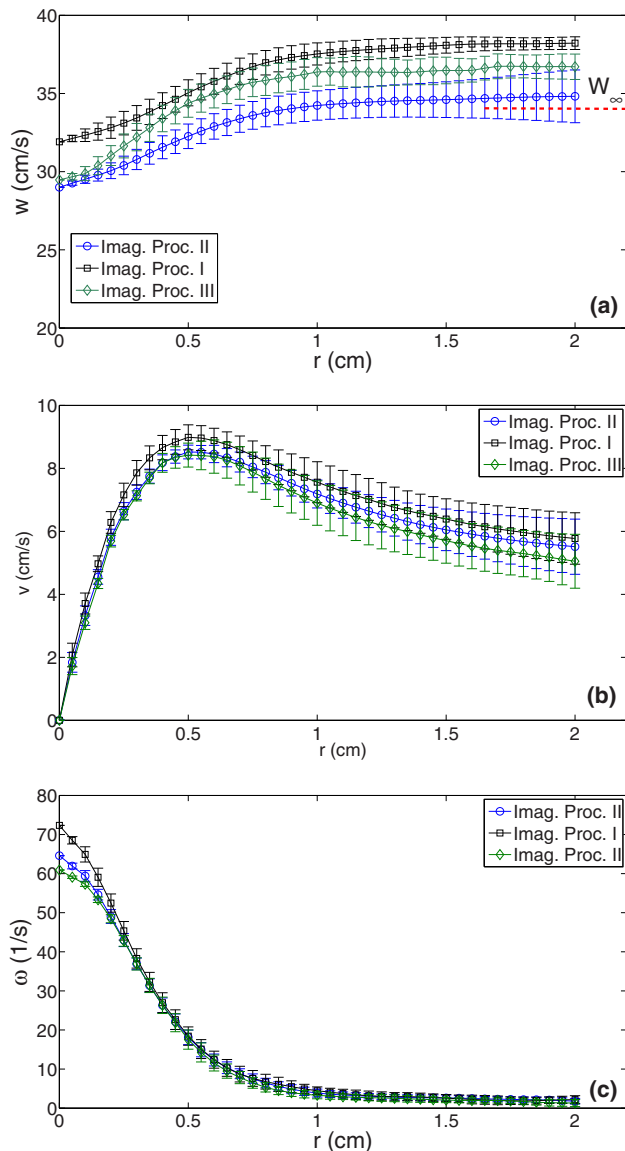

FIG. 3. (Color online) (a) Averaged radial profiles and error bars of the axial velocity component w, (b) the azimuthal velocity component v, and (c) axial vorticity component ω, as they are obtained from the three different image processing techniques mentioned in the text (numbered in the legend as I, II, and III in the order mentioned in the text), for $z/c = 3$, $Re_c = 4.27 \times 10^4$, and $\alpha = 12°$. The dashed line in (a) corresponds to the experimental value W_∞ from the calibrated flowmeter (see Fig. 2).

all the software is MATLAB-based, and, secondly, because this image processing technique has been successfully tested previously in similar (but 2D) vortex flows.[45,46] Note also in Fig. 3(a) that this technique gives the best results for the imposed axial velocity W_∞. In any case, the mean azimuthal velocity results obtained with the other two techniques are practically the same for all the cases we have considered.

As an example, Fig. 4 shows the mean vorticity fields obtained through this PIV technique at the different axial distances z/c mentioned above for $\alpha = 12°$ and the highest Reynolds number considered. Vorticity is calculated by the differentiation of a least-square spline approximation of the velocity field to avoid any undesirable effect of the differentiation of noisy field. Note that the roll-up of the vorticity is
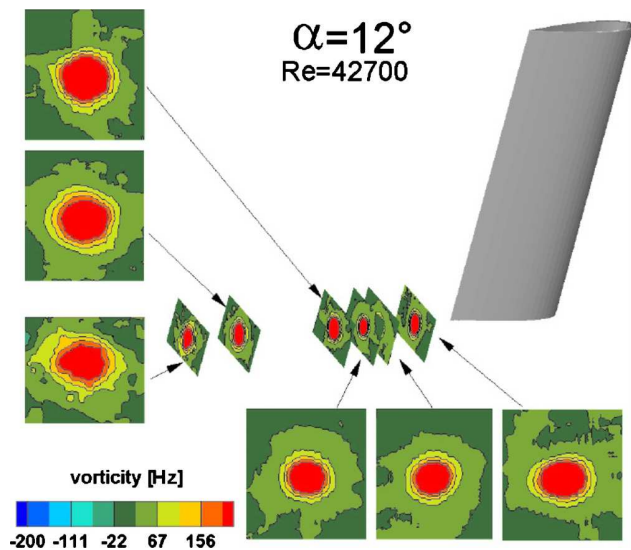
FIG. 4. (Color online) Mean vorticity fields at $z/c = 0.5, 3, 4, 6, 12.5,$ and 16 for $Re_c = 4.27 \times 10^4$ and $\alpha = 12°$.

not clearly visible in the first axial locations close to the wing tip due to this averaging process and the recentering of the PIV data, which are made in a square region (2×2 cm^2) that is not large enough to see the roll-up process. Vorticity profiles are preferred in Sec. IV below to velocity profiles for fitting to the experimental results the parameters of the different theoretical models because the mathematical expressions for vorticity in the models are much simpler.

IV. COMPARISON BETWEEN TRAILING VORTEX MODELS AND PIV MEASUREMENTS

A. Summary and discussion of theoretical models for wing tip vortices

As commented on in Sec. I, the first comprehensive model that included the axial flow in a trailing vortex was that of Batchelor.[15] This author considered the boundary-layer-type approximation of the equations of motion, $\partial/\partial z \ll \partial/\partial r$ and $u \ll w$, where (u, v, w) are the velocity components in the cylindrical polar coordinates (r, θ, z) along the vortex axis z, an approximation valid far downstream from the wing tip, supplemented by the assumption that the axial velocity defect (or excess) is small compared to the flight speed. The resulting linearized parabolic equations are solved with the boundary condition that the far field tangential velocity tends to a potential vortex, $rv \rightarrow$ constant $\equiv \Gamma_0/(2\pi)$ as $r \rightarrow \infty$, where Γ_0 is the circulation of the vortex, and the axial velocity tends to the flight speed W_∞, for which Batchelor[15] found a self-similar solution of the form

$$u(r,z) = 0, \quad v(r,z) = \frac{\Gamma_0}{2\pi r}\left[1 - e^{-W_\infty r^2/(4\nu z)}\right], \quad (2)$$

$$w(r,z) = W_\infty + \frac{\Gamma_0^2}{32\pi^2 \nu z}B\left(\frac{W_\infty r^2}{4\nu z}\right)$$
$$- \left[\frac{\Gamma_0^2}{32\pi^2 \nu}\ln\left(\frac{W_\infty z}{\nu}\right) + \frac{W_\infty^2 L}{8\nu}\right]\frac{e^{-W_\infty r^2/(4\nu z)}}{z}, \quad (3)$$

where

$$B(\xi) \equiv e^{-\xi}[\ln \xi + E_1(\xi) - 0.807] + 2E_1(\xi) - 2E_1(2\xi) \quad (4)$$

being $E_1(\xi) \equiv \int_\xi^\infty dx e^{-x}/x$ the exponential integral function,[48] and L is an integration constant with dimensions of an area. Batchelor found that this last parameter is related to the drag of the wing, and can be estimated (for an elliptic loaded wing) as[15]

$$L \sim \left(\frac{C_L s}{\pi A_R}\right)^2, \quad (5)$$

where C_L is the lift coefficient, s is the wing span, and $A_R = s^2/A$ is the aspect ratio, being A a wing reference area (for a rectangular wing, $A_R = s/c$, where c is the chord of the wing).

It is seen that the viscous core of Batchelor's vortex grows downstream as $\sqrt{\nu z/W_\infty}$. Therefore, it is convenient to use the nondimensional variables

$$\bar{r} = \frac{r}{c}, \quad \bar{z} = \frac{z}{c\,Re_c}, \quad \bar{v} = \frac{v}{W_\infty}, \quad \bar{w} = \frac{w}{W_\infty}, \quad (6)$$

where Re_c is the Reynolds number based on the wing chord c [defined in Eq. (1)], and the similarity variable

$$\eta \equiv -\frac{W_\infty r^2}{4\nu z} = -\frac{\bar{r}^2}{4\bar{z}} \quad (7)$$

so that Batchelor's vortex can be written in nondimensional form as

$$\bar{v} = \frac{S}{r}(1 - e^\eta), \quad (8)$$

$$\bar{w} = 1 + \frac{S^2}{8\bar{z}}B(-\eta) - [S^2 \ln(Re_c^2\,\bar{z}) + \delta]\frac{e^\eta}{8\bar{z}}. \quad (9)$$

In these expressions

$$S \equiv \frac{\Gamma_0}{2\pi c W_\infty} \quad (10)$$

is a swirl number, and

$$\delta \equiv \frac{L}{c^2}. \quad (11)$$

In terms of the Reynolds number based on the circulation

$$Re_\Gamma \equiv \frac{\Gamma_0}{\nu}. \quad (12)$$

S can be written as

$$S = \frac{Re_\Gamma}{2\pi\,Re_c}. \quad (13)$$

It is interesting to note that, since function B vanishes at $r=0$, Batchelor's vortex has always an axial velocity deficit at the axis, $w(r=0,z) < W_\infty$ or $\bar{w}(\bar{r}=0,\bar{z}) < 1$. This axial velocity deficit decays axially as $\bar{z}^{-1} \ln \bar{z}$ for sufficiently large $\bar{z}$ (note that δ is usually very small)

$$\Delta \bar{w} \equiv \frac{W_\infty - w(r=0,z)}{W_\infty}$$

$$= 1 - \bar{w}(\bar{r}=0,\bar{z})$$

$$\simeq \frac{S^2}{8} \bar{z}^{-1} \ln(Re_c^2 \bar{z}). \tag{14}$$

Another quantity of interest to compare with the experiments is the axial evolution of the radius at which the azimuthal velocity of the vortex is a maximum, which for Batchelor's vortex is

$$r_{\max} = 2.2418 \sqrt{\frac{\nu z}{W_\infty}} \quad \text{or} \quad \bar{r}_{\max} = 2.2418 \bar{z}^{1/2}. \tag{15}$$

Finally, it is of experimental interest the axial component of the vorticity, $\omega = (1/r) \partial(rv)/\partial r$, which in dimensionless form is given by

$$\bar{\omega} \equiv \frac{\omega c}{W_\infty} = \frac{S}{2} \frac{e^\eta}{\bar{z}} \tag{16}$$

and its axial value is

$$\bar{\omega}_0 \equiv \bar{\omega}(\bar{r}=0,\bar{z}) = \frac{S}{2\bar{z}}. \tag{17}$$

A simplified, columnar (i.e., without axial variation) version of Batchelor's vortex (8) and (9), usually called q-vortex, has been almost universally used in stability analyses of trailing vortices. Basically, it is obtained by setting $\bar{z}=1$ in Eqs. (8) and (9), but using as the characteristic velocity to render nondimensional the velocity field the axial velocity multiplying the exponential term in Eq. (3), instead of W_∞, so that the swirl number (now usually called q) and the Reynolds numbers are different from those defined in Eqs. (10) and (1). However, this is a crude idealization of the vortex, since the axial velocity at the axis used as a reference velocity evolves with z, in addition to other inconveniences shared by the full version of Batchelor's vortex which we now comment.

Batchelor's solutions (2) and (3) are valid when the characteristic radius $r_c \sim \sqrt{\nu z/W_\infty}$ of the vortex is sufficiently large. Moore and Saffman[25] estimated that it has to be a significant fraction of the wing span s

$$r_c = \epsilon s \tag{18}$$

with $\epsilon < 1$ ($\epsilon \sim 1/5$, say). Or, in terms of the wing chord c

$$r_c = \epsilon s = \epsilon A_R c = ac, \tag{19}$$

where the unknown constant a is of order unity because the aspect ratio A_R typically ranges between 7 and 10. That is to say, Batchelor's vortex is a good approximation for axial distances of the order of

$$z = (a^2/4)c\, Re_c \quad \text{or} \quad \bar{z} \sim 1 \tag{20}$$

or larger. This means that, typically, z must be of the order of several thousand chord lengths. This fact makes Batchelor's vortex unrealistic for modeling trailing vortices,[25] and, as stated by Spalart[2] "it is unfortunate that this q-vortex is used almost universally in stability studies."

For these reasons, Moore and Saffman[25] developed a somewhat more realistic laminar model for trailing vortices which, though also asymptotically valid far downstream, it is a good approximation just a few chords downstream, once the roll-up process has finished. To that end, they also solved, as it was done by Batchelor, the boundary-layer-type equations for the axial velocity induced by the viscous decay of the swirl, but, instead of assuming an external potential vortex like in Batchelor's solution, Moore and Saffman considered a more realistic solution for the external inviscid swirl that takes into account the roll-up process.

In particular, Moore and Saffman applied the Betz[49] method (see also Ref. 50) to complete the solution of Kaden[51] for the class of vortex sheets with circulation distribution along the wing span $\Gamma(x) \sim x^{1-n}$, $0 < n < 1$, where x is the coordinate in from the tip ($n=1/2$ represents the sheet near the tip of an elliptically loaded wing). These power-law distributions roll up into vortices having the inviscid circulation distribution around the wing tip vortex $\Gamma(r) = \Gamma(\lambda x)$, where the Betz model was used to determine that $\lambda = 2-n$. For $n > 0$, the swirl goes to infinity at the center of the vortex, $v \sim r^{-n}$, and its regularization by viscosity yields the similarity solution of Moore and Saffman.

In terms of the nondimensional variables (6), Moore and Saffman solution for the azimuthal velocity can be written as

$$\bar{v}(\bar{r},\bar{z}) = \frac{b}{\bar{z}^{n/2}} V_n(\eta), \tag{21}$$

where b is a nondimensional constant related to the circulation, and

$$V_n(\eta) = 2^{-n} \Gamma\left(\tfrac{3}{2} - \tfrac{1}{2}n\right)(-\eta)^{1/2} M\left(\tfrac{1}{2} + \tfrac{1}{2}n; 2; \eta\right) \tag{22}$$

with Γ the gamma function (not to be confused with the circulation) and M the confluent hypergeometric function of the first kind.[48] For large $\bar{r}$

$$\bar{v} \to b\bar{r}^{-n} \quad \text{as} \quad \bar{r} \to \infty \tag{23}$$

and the maximum of $\bar{v}$ is located at

$$\bar{r}_{\max} = 2(\eta_n \bar{z})^{1/2}, \tag{24}$$

where η_n is a parameter that depends on n (e.g., $\eta_n \simeq 2.13$ for $n=1/2$).[25]

The nondimensional axial velocity is

$$\bar{w} = 1 + \frac{b^2}{\bar{z}^n} W_n(\eta). \tag{25}$$

$W_n(\eta)$ being the solution to an ordinary differential equation,[25] and with the axial velocity defect at the axis
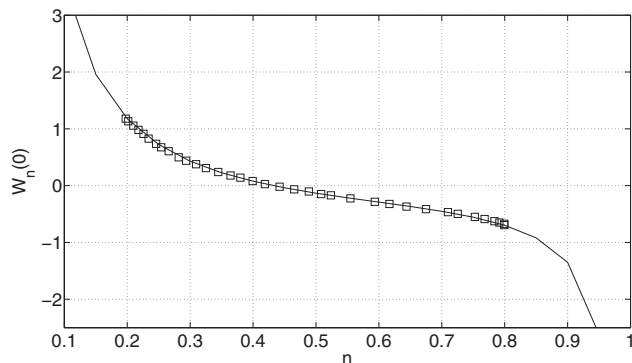
FIG. 5. Computed $W_n(0)$ vs n, compared to Fig. 2 of Moore and Saffman (Ref. 25) (squares).

$$\Delta \bar{w} \equiv 1 - \bar{w}(\bar{r} = 0, \bar{z}) = -W_n(0)\frac{b^2}{\bar{z}^n}, \tag{26}$$

where constant $W_n(0)$ is given in Fig. 5 as a function of n. It is interesting to note that $W_n(0)$ changes its sign for $n \simeq 0.44$, being negative for $n > 0.44$, so that, according to the solution by Moore and Saffman, an axial velocity defect will develop only for $n > 0.44$.

The nondimensional vorticity is

$$\bar{\omega} = \frac{b}{r\bar{z}^{n/2}}\Omega_n(\eta), \tag{27}$$

$$\Omega_n(\eta) = 2^{-n}\Gamma\left(\tfrac{3}{2} - \tfrac{1}{2}n\right)\left[2(-\eta)^{1/2}M\left(\tfrac{1}{2} + \tfrac{1}{2}n; 2; \eta\right) \\ - \left(\tfrac{1}{2} + \tfrac{1}{2}n\right)(-\eta)^{3/2}M\left(\tfrac{3}{2} + \tfrac{1}{2}n; 3; \eta\right)\right] \tag{28}$$

which at the axis is given by

$$\bar{\omega}_0 \equiv \bar{\omega}(\bar{r} = 0, \bar{z}) = \frac{2^{-n}\Gamma\left(\tfrac{3}{2} - \tfrac{1}{2}n\right)b}{\bar{z}^{(n+1)/2}}. \tag{29}$$

In addition to the above laminar flow studies, there have been several attempts to develop turbulent models for the structure and decay of trailing vortices, being the most significant one that of Saffman,[52,53] which is an extension of an earlier work by Govindaraju and Saffman.[54] One of the main features of these solutions is the prediction of a mean circulation distribution that is not monotonic with increasing radius, i.e., a circulation overshoot. Govindaraju and Saffman[54] show by very simple arguments that this is a necessary feature of a turbulent vortex if the turbulent stresses decay more rapidly than the viscous stresses and the core radius grows more rapidly than $(\nu t)^{1/2}$. Although this overshoot has never been observed experimentally, fully turbulent vortices have not been studied under controlled conditions. Saffman[52] developed a more complex structure for the turbulent vortex, including the axial velocity, to explain the observed dependence of turbulent line vortices on Reynolds number.

There exists some other models for turbulent tip vortices in the literature, but they are semiempirical models which are not based on the turbulent flow equations and, consequently, they do not model the axial evolution or decay of these vor-

tices. For these reason we will compare our experimental results only with the laminar vortex models by Batchelor and by Moore and Saffman.

B. Comparison with the experimental results and discussion

We compare here the two models for laminar trailing vortices discussed in the preceding subsection with the PIV measurements reported in Sec. III. As mentioned in that section, vorticity is preferred to fit the experimental data to the models because the model expressions for the vorticity are the simplest ones. However the resulting fitting parameters would be practically the same if the azimuthal velocity profiles were used because the dispersion in the azimuthal velocity profiles and in the vorticity profiles are quite similar (see below).

Figure 6 shows such a comparison for $\alpha = 12$, $Re_c \simeq 4 \times 10^4$, and the different values of z/c considered (see Fig. 2). We use a Levenberg–Marquardt algorithm built in MATLAB for the fittings. It is clear that the self-similar solution of Moore and Saffman (MS for short) fits much better to the experimental data than the one by Batchelor (B). This is so for all the cases considered, as it was expected because B model is valid only very far downstream from the wing tip, as discussed in the preceding subsection. The mathematical reason is that the MS model contains an additional parameter (power n) in relation to the B model, so that it permits the fitting of a larger variety of velocity profiles than the B model. This is particularly clear in the tails of the vorticity profiles, which for the values of r/c depicted in Fig. 6 do not decay as the power r^{-1} required by the B model, but with a different power r^{-n}. This conclusion is even clearer when the azimuthal velocity profiles are used to compare the models with the experimental data (see Fig. 7).

We have fitted the experimental vorticity (and azimuthal velocity) profiles to the self-similar models by adjusting the best fitting parameters in these models, namely, the swirl parameter S in B, the power n, and the parameter b in MS. In addition, we have also adjusted in each case the best fitting axial locations $\bar{z} - \bar{z}_{0B}$ and $\bar{z} - \bar{z}_{0MS}$ in the self-similar variable of each model, in such a way that the axial origins are displaced to the virtual origins $\bar{z}_{0B}$ and $\bar{z}_{0MS}$ in B and MS self-similar solutions, respectively. The physical justification is that the axial (streamwise) origin in these self-similar solutions is not defined, and depends on the roll-up process behind the wing tip. One has the liberty to select these virtual origins as an additional parameter in the self-similar models. By doing so one obtains a much better fit to the experimental data (e.g. Figs. 6 and 7). In addition, one finds that the resulting values of $\bar{z}_{0B}$ and $\bar{z}_{0MS}$ remain practically constant for all the configurations and axial distances z/c considered (see Fig. 8). This fact justifies the appropriateness of using these virtual origins, which in the present case are $\bar{z}_{0B} \simeq -6.4 \times 10^{-4}$ and $\bar{z}_{0MS} \simeq -2.2 \times 10^{-4}$, respectively. Similar virtual origins for self-similar solutions have been used and justified theoretically by Revuelta et al.[55] in the case of laminar jets.

The power n in the MS model fluctuates around a mean value due to the experimental dispersion (see Fig. 9). Note
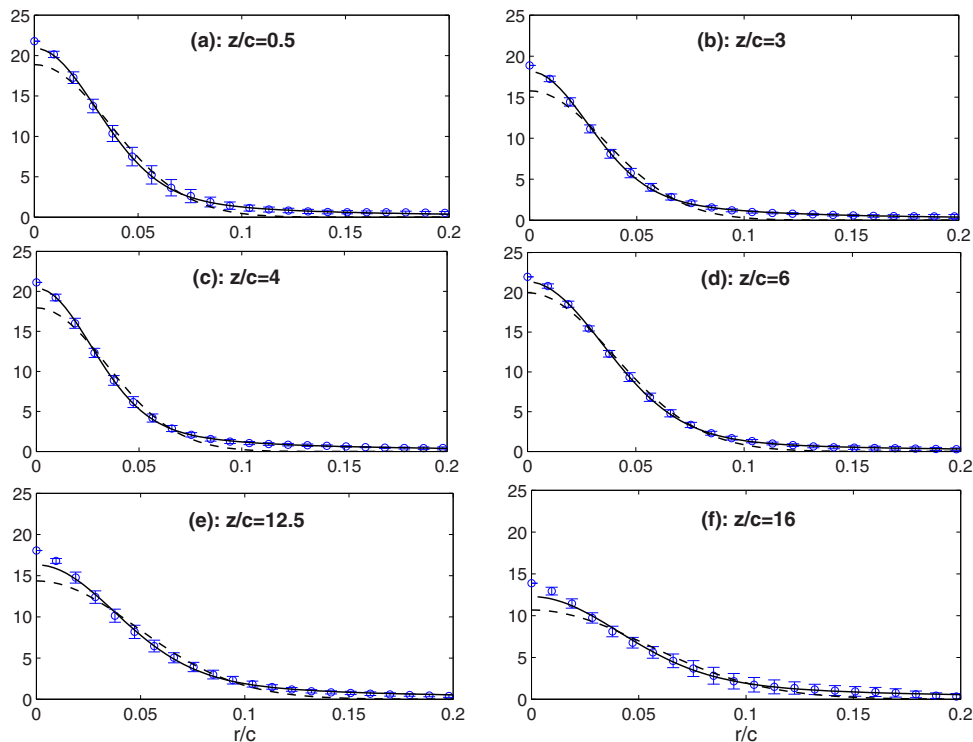
FIG. 6. (Color online) Comparison between the nondimensional vorticity $\bar{\omega} = \omega c / W_\infty$ obtained experimentally (dots) with the best fitted solutions by Batchelor [dashed lines, Eq. (16)], and Moore and Saffman [continuous lines, Eq. (27)], for $\alpha = 12°$, $Re_c \simeq 4 \times 10^4$, and different values of z/c, as indicated.

also that the fitting process to the MS model is more involved than the fitting to the B one because the MS model is more complex. We can select a mean value $n \simeq 0.54$ for all the cases considered. Of course, this power may be very

sensitive to the geometry of the wing, and, possibly, another different mean value may result if a different wing model would have been used in the experiments. Finally, the parameters b in the MS model and S in the B model approximately
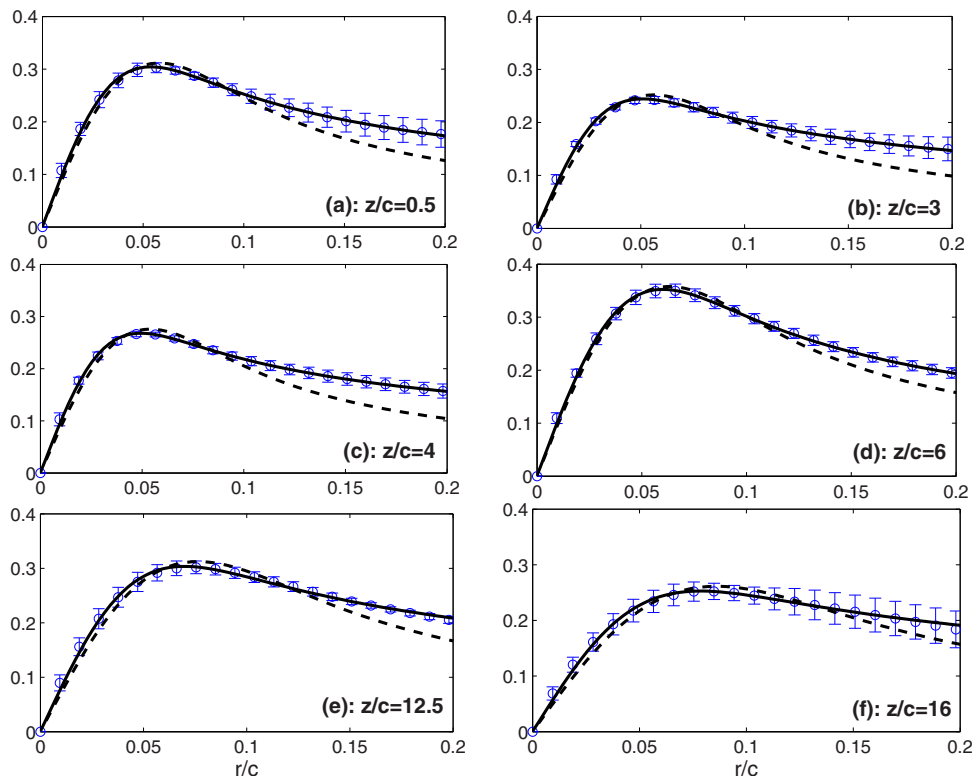

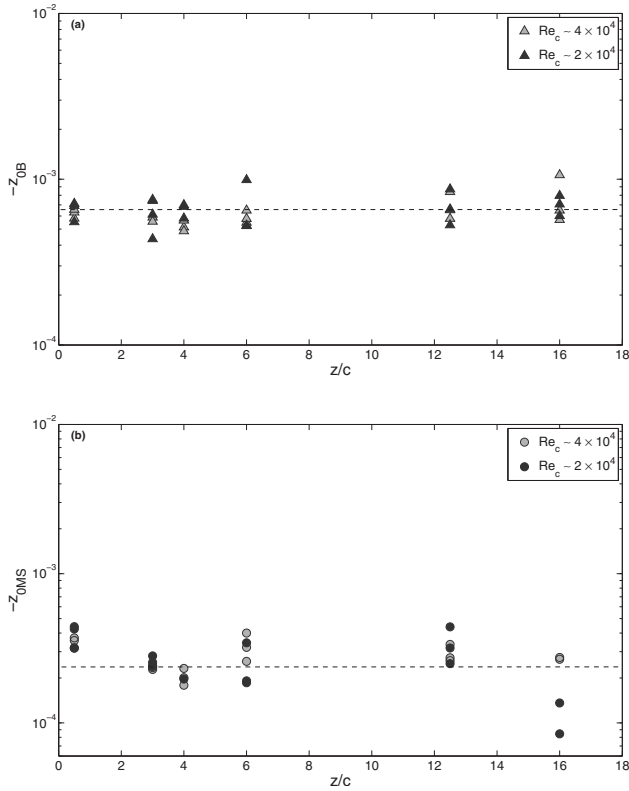FIG. 7. (Color online) As in Fig. 6, but for the nondimensional azimuthal velocity $\bar{v} = v / W_\infty$.

FIG. 8. Virtual origins of the (a) B model $-\bar{z}_{0B}$ and the (b) MS model $-\bar{z}_{0MS}$ vs z/c for the different values of Re_c and α considered. The dashed lines represent the average values.

FIG. 10. (a) b/α and S/α vs z/c for the different values of Re_c and α considered. (b) b/α and S/α vs α for the different values of Re_c and z/c considered; the dashed lines correspond to the average values for large z/c.

tend to constants as z/c increases when they are scaled with α [see Fig. 10(a)]. This is explained by the fact that both parameters are proportional to the circulation (see previous section),

which in turn is proportional to the wing angle of attack. According to these figures, we can select $b/\alpha \simeq 7.5 \times 10^{-3}$ and $S/\alpha \simeq 3.5 \times 10^{-3}$ for the comparison with the present experimental results [see Fig. 10(b)].

The situation is rather different for the axial velocity profiles. Figure 11 shows that the MS model does not agree so well with the axial velocity profiles measured experimentally as the azimuthal velocity, or the vorticity, does (note
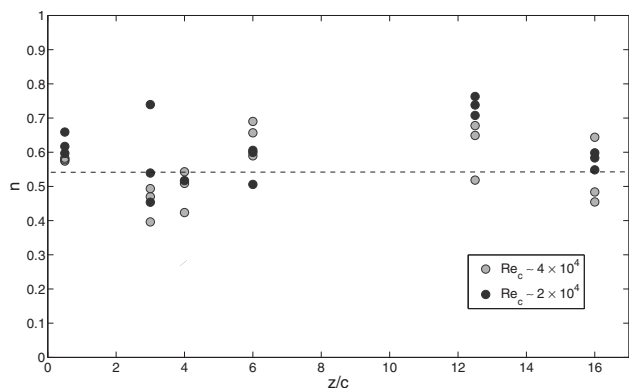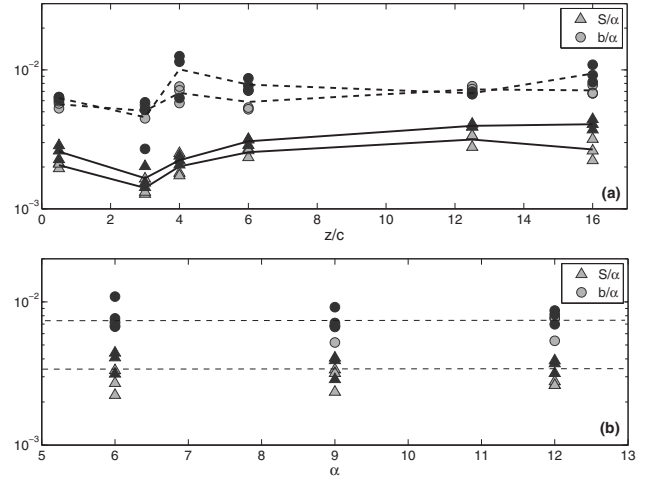

FIG. 9. Power n in MS model vs z/c for the different values of Re_c and α considered.

that the best fitting parameters in the models are obtained from the vorticity or the azimuthal velocity profiles). However the disagreement with the B model is quite pronounced. This is a clear evidence of the fact that the assumptions behind the B model are valid very far downstream of the wing, as discussed in the previous subsection. Thus, the axial velocity defect at the axis given by the B model behaves as $\bar{z}^{-1} \ln \bar{z}$ for $\delta=0$ [see Eq. (14)], which is much larger than the experimental results for the values of $\bar{z}$ considered (see also Fig. 14 below). Although we have used $\delta=0$ in the B model, because it is usually very small compared to $S^2 \ln(Re_c^2 \bar{z})$ in Eq. (9), the comparison with the experimental data would be even worse if some (small) values of δ were used in the B model.

In addition to the fitting of the radial profiles of the vorticity and the velocity, at a given axial location, to the self-similar solutions, it is relevant to check whether these solutions predict correctly the streamwise variation of the vortices. As it was seen in Sec. IV A, there are several nondimensional magnitudes which are appropriate to perform this comparison, such as the nondimensional vorticity at the axis, $\bar{\omega}_0$, which is a measure of the vortex strength, the nondimensional radius where the azimuthal velocity reaches its maximum, $\bar{r}_{max}$, which is a measure of the vortex core radius, and the nondimensional axial velocity defect at the axis, $\Delta \bar{w}$. According to the two models described in the above section, the axial profiles of these nondimensional magnitudes are independent of the Reynolds number when plotted against the nondimensional axial coordinate $\bar{z}$ [see Eqs. (6), (14), (15), (17), (24), (26), and (29)]. Another nondimensional magnitude that may characterize the vortex strength is $\bar{v}_{max}/\bar{r}_{max}$, but we have checked that the resulting fitting parameters are quite similar to those obtained with $\bar{\omega}_0$, and we prefer this last one for simplicity.

Figure 12 shows the nondimensional radius at which the azimuthal velocity reaches a maximum, $\bar{r}_{max}$, as a function of the nondimensional axial distance $\bar{z}$. Note that, although the physical axial locations of the normal planes where PIV mea-
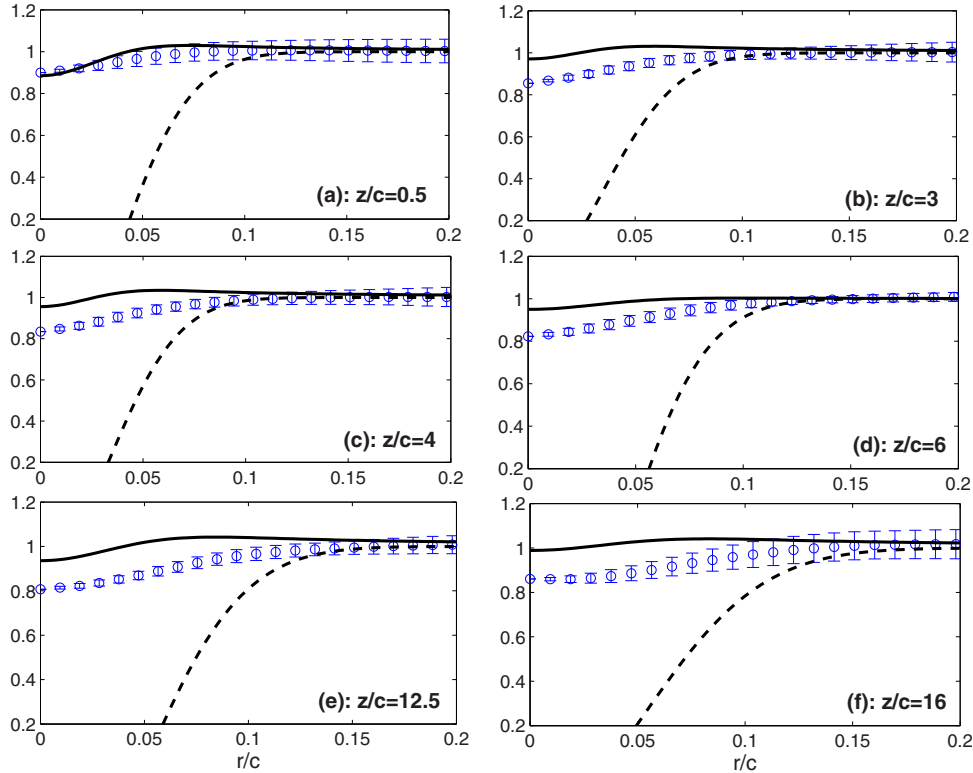
FIG. 11. (Color online) As in Fig. 6, but for the nondimensional axial velocity $\bar{w} = w/W_\infty$.

surements are captured are the same for the two Reynolds numbers, the values of $\bar{z}$ are twice for the smallest Reynolds considered [see Eq. (6) for the definition of $\bar{z}$]. According to both models, B and MS, this radius grows as $\bar{z}^{1/2}$ [see Eqs. (15) and (24)], independently of the Reynolds number (as all the nondimensional magnitudes), and also independently of the vortex strength (parameter S or b). We use the mean value $n = 0.54$ in the MS model. Because the use of a virtual origin in both models, the axial coordinate for the model curves in the figure are $\bar{z} - \bar{z}_{0B}$ and $\bar{z} - \bar{z}_{0MS}$ for the B and MS models, respectively, so that the behavior $\bar{z}^{1/2}$ is reached asymptotically for sufficiently large $\bar{z}$. In Fig. 12 this tendency is observed for $\bar{z}$ larger than 10^{-3}, which is larger than the maximum value at which experimental data are captured in this work. Therefore, we cannot decide which model fits better to the present experimental results for $\bar{r}_{\max}(\bar{z})$, although the agreement is quite good with both models up to the maximum value of $\bar{z}$ considered. Note that although the tails of the azimuthal velocity radial profiles are better captured by the MS model (see Fig. 7), both models are similarly valid close to $\bar{r}_{\max}$.

Figure 13 shows the experimental values of $\bar{\omega}_0$, scaled with the angle of attack α, plotted against $\bar{z}$ for the two Reynolds numbers and the three angles of attack considered, comparing them with the expressions (17) and (29) for the B and MS models, respectively, divided by α. The values of the parameters in the models are the mean ones for S/α, b/α, and n discussed above. Both solutions predict practically the same evolution for $\bar{\omega}_0/\alpha$ in the range of $\bar{z}$ considered when the virtual origins are used. Again, the values of $\bar{z}$ where the

experimental data are captured are too small to decide whether they fit better to the asymptotic behavior $\bar{z}^{-1}$ of the B model (17), or to the behavior $\bar{z}^{-(n+1)/2}$ of the MS model (29). However, as noted above, the details of the radial profiles of the vorticity at each streamwise location are much better predicted by the MS model than by the B model (see Fig. 6).

Finally, Fig. 14 plots the values of $\Delta \bar{w}$ obtained experimentally as a function of $\bar{z}$, and compare them to the two models with the parameters S, n, and b given in the legend (S and b are the mean values of S/α and b/α discussed above multiplied by the extreme values of α). For the mean value $n = 0.54$ used, the parameter $W_n(0)$ in the MS model
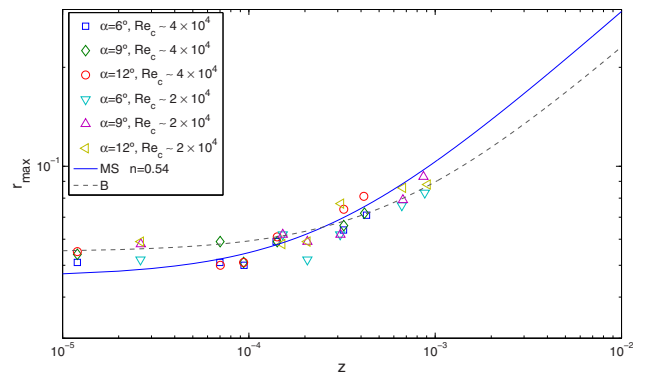

FIG. 12. (Color online) Nondimensional radius where the azimuthal velocity reaches a maximum ($\bar{r}_{\max}$) vs $\bar{z}$ obtained experimentally (symbols) for all the cases considered (as indicated in the legend), and their comparison to the models of Batchelor (B) and that by Moore and Saffman (MS) for $n = 0.54$.
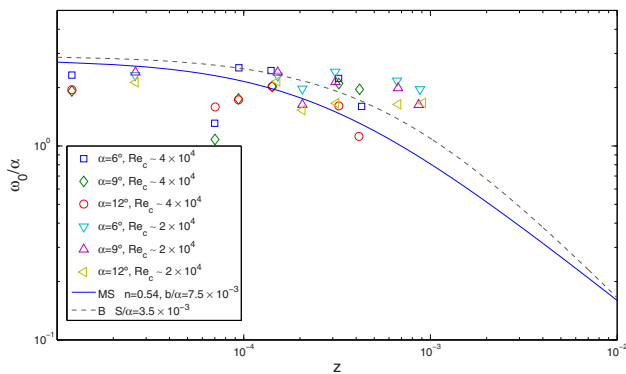
FIG. 13. (Color online) Nondimensional vorticity at the axis scaled with α, $\overline{\omega}_0/\alpha$ vs $\overline{z}$ measured experimentally (symbols) for the two Reynolds number and three values of α considered (as indicated in the legend), and their comparison to different models with the indicated parameters.

appearing in Eq. (26) is $Wn(0) \simeq -0.3$, so that the radial profile of the axial velocity component in the MS model is wakelike, as it happens in all the profiles measured experimentally [e.g., Figs. 3(a) and 11]. As in the previous figures, it is difficult to decide which model predicts better the downstream evolution of the axial velocity defect because the small values of $\overline{z}$ in the experimental data. However, the MS model clearly yields much better the order of magnitude of $\Delta\overline{w}$ along $\overline{z}$ obtained in the experiments.

V. SUMMARY AND CONCLUSIONS

We have undertaken a series of measurements of the 3D velocity field of the trailing vortex behind a NACA 0012 airfoil using a stereo PIV technique. We have considered two different Reynolds numbers (2 and 4×10^4, approximately), three angles of attack (6°, 9°, and 12°), and six axial distances from the wing tip, ranging from 0.5 to 16 chord lengths. We have made a comprehensive review on the literature about theoretical models for the structure of trailing vortices, paying special attention to those viscous models that include the axial velocity component and consider the downstream evolution along the vortex axis of the velocity field. This last point is important because the viscous insta-
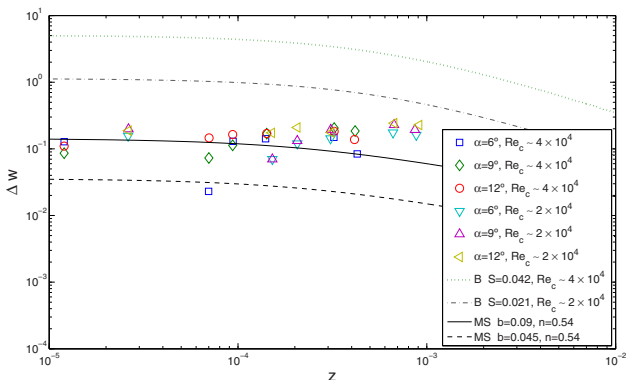
bilities of vortices, relevant for the prediction of trailing vortex dynamics and decay, are strongly affected by the axial flow and by the velocity evolution along the vortex axis.

In particular, we have compared our experimental results with the models (self-similar solutions) by Batchelor[15] and by Moore and Saffman.[25] We find that the radial profiles of both the azimuthal and axial velocity components on a normal plane to the vortex axis fit better to the model by Moore and Saffman in all the axial locations considered, provided that a virtual origin $\overline{z}_{0MS} \equiv z_{0MS}/(c\,Re_c) \simeq -2.2 \times 10^{-4}$ is used for the nondimensional axial distance. Actually, Batchelor's model predicts quite poorly the radial profiles of the axial velocity at the downstream distances considered, especially the axial velocity defect at the axis, in consonance with the fact that the hypotheses behind this model are valid very far downstream the wing tip.

We have also compared the streamwise variation of some relevant features of the vortex with the predictions from both models. We find that, up to the maximum axial distance considered in the experiments, both models agree reasonably well, within experimental dispersion, with the experimental data for the evolutions of the vortex strength (maximum of vorticity) and the vortex core radius. However, these axial distances are shown to be too small to decide which of the models fits better to the downstream evolution of the vortex, in spite of the fact that we have captured the 3D velocity field up to 16 chords, which is the maximum axial distance for PIV measurements available in our experimental facility. Although one may increase the nondimensional axial distance $\overline{z}$ by reducing the Reynolds number, the needed of Re_c would be too low for practical interest. Therefore, detailed experimental measurements farther downstream of the wing tip than the ones reported in the present work would be needed to shed more light on this question.

FIG. 14. (Color online) Nondimensional axial velocity defect at the axis ($\Delta\overline{w}$) vs $\overline{z}$ obtained experimentally for all the cases considered (as indicated in the legend), and their comparison to the models with the indicated parameters.

[1] S. E. Widnall, "The structure and dynamics of vortex filaments," Annu. Rev. Fluid Mech. **7**, 141 (1975).
[2] P. Spalart, "Airplane trailing vortices," Annu. Rev. Fluid Mech. **30**, 107 (1998).
[3] Th. Gerz, F. Holzapfel, and D. Darracq, "Commercial aircraft wake vortices," Prog. Aerosp. Sci. **38**, 181 (2002).
[4] L. Jacquin, D. Fabre, P. Gefroy, and E. Coustols, "The properties of a transport aircraft wake in the extended near field: An experimental study," AIAA Paper No. 2001-1038, 2001.
[5] Th. Gerz, F. Holzapfel, W. Bryant, F. Kopp, M. Frech, A. Tafferner, and G. Winckelmans, "Research toward a wake-vortex advisory system for optimal aircraft spacing," C. R. Phys. **6**, 501 (2005).
[6] A. Allen and C. Breitsamter, "Experimental investigation of counter-rotating four vortex aircraft wake," Aerosp. Sci. Technol. **13**, 114 (2009).
[7] H. Deniau and L. Nybelen, "Strategy for spatial simulation of co-rotating vortices," Int. J. Numer. Methods Fluids **61**, 23 (2009).
[8] D. Fabre and L. Jacquin, "Short-wave cooperative instabilities in representative aircraft vortices," Phys. Fluids **16**, 1366 (2004).
[9] D. Fabre and L. Jacquin, "Viscous instabilities in trailing vortices at large swirl numbers," J. Fluid Mech. **500**, 239 (2004).

[10] S. Le Dizès and D. Fabre, "Large-Reynolds-number asymptotic analysis of viscous centre modes in vortices," J. Fluid Mech. **585**, 153 (2007).

[11] L. Parras and R. Fernandez-Feria, "Spatial stability and the onset of absolute instability of Batchelor's vortex for high swirl numbers," J. Fluid Mech. **583**, 27 (2007).

[12] D. Fabre and S. Le Dizes, "Viscous and inviscid center modes in vortices: The vicinity of the neutral curves," J. Fluid Mech. **603**, 1 (2008).

[13] C. Roy, N. Schaeffer, S. Le Dizes, and M. Thompson, "Stability of a pair of co-rotating vortices with axial flow," Phys. Fluids **20**, 094101 (2008).

[14] S. I. Green, in *Fluid Vortices*, edited by S. I. Green (Kluwer, Dordrecht, 1995), pp. 317–372.

[15] G. K. Batchelor, "Axial flow in trailing line vortices," J. Fluid Mech. **20**, 645 (1964).

[16] R. L. Ash and M. R. Khorrami, in *Fluid Vortices*, edited by S. I. Green (Kluwer, Dordrecht, 1995), pp. 317–372.

[17] M. Lessen, P. J. Singh, and F. Paillet, "The stability of a trailing line vortex. Part 1. Inviscid theory," J. Fluid Mech. **63**, 753 (1974).

[18] M. Lessen and F. Paillet, "The stability of a trailing line vortex. Part 2. Viscous theory," J. Fluid Mech. **65**, 769 (1974).

[19] E. W. Mayer and K. G. Powell, "Viscous and inviscid instabilities of a trailing vortex," J. Fluid Mech. **245**, 91 (1992).

[20] C. Olendraru and A. Sellier, "Viscous effects in the absolute-convective instability of the Batchelor vortex," J. Fluid Mech. **459**, 371 (2002).

[21] C. J. Heaton, "Center modes in inviscid swirling flows and their application to the stability of the Batchelor vortex," J. Fluid Mech. **576**, 325 (2007).

[22] W. McCormick, J. L. Tangler, and H. E. Sherrier, "Structure of trailing vortices," J. Aircr. **5**, 260 (1968).

[23] J. H. Olsen, *Aircraft Wake Turbulence and Its Detection* (Plenum, New York, 1971), p. 445.

[24] G. R. Baker, S. J. Barker, K. K. Bofah, and P. G. Saffman, "Laser anemometer measurements of trailing vortices in water," J. Fluid Mech. **65**, 325 (1974).

[25] D. W. Moore and P. G. Saffman, "Axial flow in laminar trailing vortices," Proc. R. Soc. London, Ser. A **333**, 491 (1973).

[26] E. Chadwick, "The vortex line in steady, incompressible Oseen flow," Proc. R. Soc. London, Ser. A **462**, 391 (2006).

[27] D. Birch, T. Lee, F. Mokhtarian, and F. Kafyeke, "Structure and induced drag of a tip vortex," J. Aircr. **41**, 1138 (2004).

[28] G. Lombardi and P. Skinner, "Wing tip vortex in the near field: An experimental study," J. Aircr. **42**, 1366 (2005).

[29] C. Karakus, H. Akilli, and B. Sahin, "Formation, structure, and development of near-field wing tip vortices," J. Aerosp. Eng. **222**, 13 (2008).

[30] D. Birch, T. Lee, F. Mokhtarian, and F. Kafyeke, "Rollup of near-field behavior of a tip vortex," J. Aircr. **40**, 603 (2003).

[31] W. J. Devenport, M. C. Rife, S. I. Liapis, and G. J. Follin, "The structure and development of a wing tip vortex," J. Fluid Mech. **312**, 67 (1996).

[32] C. Roy, "Dynamique et stabilité de tourbillons avec écoulement axial," Ph.D. thesis, Uniniversité de Provence Aix-Marseille I, Marseille (France), 2008.

[33] S. K. Iungo, P. Skiner, and G. Buresti, "Correction of wandering smoothing effects on static measurements of a wing tip vortex," Exp. Fluids **46**, 435 (2009).

[34] S. C. C. Bailey and S. Tavoularis, "Measurements of the velocity field of a wing tip vortex, wandering in grid turbulence," J. Fluid Mech. **601**, 281 (2008).

[35] S. I. Green and A. J. Acosta, "Unsteady flow in trailing vortices," J. Fluid Mech. **227**, 107 (1991).

[36] J. Fontane, P. Brancher, and D. Fabre, "Stochastic forcing of the Lamb–Oseen vortex," J. Fluid Mech. **613**, 233 (2008).

[37] D. Fabre, J. Fontane, P. Brancher, S. Le Dizes, C. Roy, T. Leweke, R. Fernandez-Feria, L. Parras, and C. del Pino, "Synthesis on vortex meandering," Technical Report No. D.1.1.1, STREP project no. AST4-CT-2005-012238, May 2008.

[38] M. L. Beninati and J. S. Marshall, "An experimental study of the effect of free-stream turbulence on a trailing vortex," Exp. Fluids **38**, 244 (2005).

[39] C. del Pino, J. M. Lopez-Alonso, L. Parras, and R. Fernandez-Feria, "Dynamics of the wing tip vortex in the near field of a NACA0012 airfoil," Aeronaut. J. (in press).

[40] J. Westerweel, "Fundamentals of digital particle image velocimetry," Meas. Sci. Technol. **8**, 1379 (1997).

[41] M. Raffel, C. Willert, and J. Kompenhans, *Particle Image Velocimetry: A Practical Guide*, 2nd ed. (Springer, Berlin, 2002).

[42] R. J. Adrian, "Twenty years of particle image velocimetry," Exp. Fluids **39**, 159 (2005).

[43] *TSI Insight 3G Software Manual* (Shoreview, Minnesota, 2006).

[44] P. Meunier and T. Leweke, "Analysis and minimization of errors due to high gradients in particle image velocimetry," Exp. Fluids **35**, 408 (2003).

[45] P. Meunier, S. Le Dizes, and T. Leweke, "Physics of vortex merging," C. R. Phys. **6**, 431 (2005).

[46] P. Meunier, C. Eloy, R. Lagrange, and F. Nadal, "A rotating fluid cylinder subject to weak precession," J. Fluid Mech. **599**, 405 (2008).

[47] D. Di Florio, F. Di Felice, and G. P. Romano, "Windowing, reshaping, and reorientation interrogation windows in particle image velocimetry for the investigation of shear flows," Meas. Sci. Technol. **13**, 953 (2002).

[48] M. Abramowitz and I. A. Stegun, *Handbook of Mathematical Functions* (Dover, New York, 1965).

[49] A. Betz, "Verhalten von Wirbelsystemen (English traslation. Behaviour of vortex systems, NACA TM 713)," Z. Angew. Math. Mech. **12**, 164 (1932).

[50] C. duP. Donaldson and A. J. Bilanin. "Vortex wakes of conventional aircraft," Technical Report No. AGARD-AG-204, NATO, 1975.

[51] H. Kaden, "Aufwicklung einer unstabilen unstetigkeitsflache," Ing.-Arch. **2**, 140 (1931).

[52] P. G. Saffman, "Structure of turbulent line vortices," Phys. Fluids **16**, 1181 (1973).

[53] P. G. Saffman, "The structure and decay of trailing vortices," Arch. Mech. **26**, 423 (1974).

[54] S. P. Govindaraju and P. G. Saffman, "Flow in a turbulent trailing vortex," Phys. Fluids **14**, 2074 (1971).

[55] A. Revuelta, A. L. Sánchez, and A. Liñán, "The virtual origin as a first-order correction for the far-field description of laminar jets," Phys. Fluids **14**, 1821 (2002).